Original Research Paper

IJES *Iranian Journal of Earth Sciences*
Vol. 14, No. 4, 2022, 301-321.
DOI: 10.30495/ijes. 2022.1942724.1660

Investigation of alterations and lineaments in Rashid-Abad mineral area (N Zanjan, NW Iran), Using integration of Remote Sensing and Aeromagnetic data

Mahsa Seyyedi[1], Mohammad Lotfi[*1], Arash Gourabjeripour[1], Afshin Ashja Ardalan[1]

1. Department of Geology, North Tehran Branch, Islamic Azad University, Tehran, Iran

Received 17 October 2021; accepted 24 January 2022

Abstract

In this research, remote sensing and aeromagnetic data sets were integrated to investigate structural features and alteration zones of Rashid-Abad mining area. This area is located approximately 45 km north of Zanjan, in the Alborz (western)-Azerbijan zone, NW Iran. For this reason, two main lineaments with the E-W and NW-SE trends were detected using a sun-angle filter of OLI data and, analytic signal (AS) and first-order vertical derivative (FVD) techniques of aeromagnetic data. The other lineaments with other trends in the area are controlled by the same two major lineaments. In order to identify alterations, the methods of band ratio (BR) in ETM+ and OLI, false-color composite (FCC), relative absorption band depth (RBD), and spectral angle mapper (SAM) in ASTER image processing were used in the study area. The results showed the presence of iron oxide, argillic, phyllic, propylitic, and silicic alterations. Also, the area's aeromagnetic response to different alteration regions was investigated by matching aeromagnetic anomalies with alteration zones. In addition, it was concluded that, iron oxide alterations with negative magnetic anomalies, phyllic alterations with moderate positive magnetic anomalies, and also argillic and silicic alterations with moderate to increasing positive magnetic anomalies were associated. Also, propylitic alterations did not show a significant relationship with magnetic values.

Keywords: *Rashid-Abad mineral area (Rashtabad), Remote sensing, Aeromagnetic data, Alterations, Lineaments.*

1. Introduction

Remote sensing is the science of acquiring, processing, and interpreting images and related data obtained from aircraft and satellite that record the interaction between matter and electromagnetic energy (Sabins 1999). RS data are used for mineral exploration in two applications: (1) map geology, and the faults and fractures that localize ore deposits; (2) recognize hydrothermally altered rocks by their spectral signatures (Sabins 1999). Generally, remote sensing has an important role in exploration of mineral deposits, lithological mapping, and detection of associated hydrothermal mineralization (e.g., Sabins 1999; Mars and Rowan 2006; Gersman et al. 2008; Amer et al. 2012; Alimohammadi et al. 2015; Manuel et al. 2017; Yazdi et al. 2018; Baratian et al. 2018; Githenya et al. 2019; Zamyad et al. 2019; Fakhari et al. 2019; Shi et al. 2020, El-Desoky et al. 2021; Mehdikhani and Imamalipour 2021; Masoumi et al. 2021; Teshnizi et al. 2021; Frutuoso et al. 2021; Yazdi et al. 2022). Landsat 7 satellite is equipped with ETM+ (Enhanced Thematic Mapper Plus) sensor. It was launched by NASA in 1999, which provides a ground survey in four modes: VNIR (Visible and Near Infrared), SWIR (Shortwave Infrared), PAN (Panchromatic), and TIR (Thermal infrared). Landsat 8 satellite is the eighth satellite of American Landsat satellite series, which launched on February 11, 2013. The Landsat 8 satellite payload consists of two science instruments: OLI (Operational Land Imager) and TIRS (Thermal Infrared Sensor) sensors. Han et al. (2018) extracted geologic lineaments in a loess area in northern Baoji based on DEM and Landsat 8 OLI remote sensing images. Terra satellite carries a payload of five remote sensors. ASTER (Advanced Spaceborne Thermal Emission and Reflection Radiometer) is one of the five sensors on-board the Terra platform which was launched by NASA in 1999. This sensor uses three different sensor subsystems: Visible and Near Infrared (VNIR), Shortwave Infrared (SWIR) and Thermal Infrared (TIR), which covers 14 multi-spectral bands from visible to thermal infrared. The Landsat7 (ETM+), Landsat 8 (OLI/TIRS), and ASTER are described in detail in Testa et al. (2018) and are summarized in Figure 1 and Table 1. Masoumi and Ranjbar (2011) used multispectral images of ETM+ and ASTER data for determining the altered areas (phyllic and propylitic zones) by using different image processing methods (the northern half of the Baft 1:100000 geological map, Iran). Lithological and hydrothermal alteration mapping of epithermal, porphyry, and tourmaline breccia (in the Argentine Andes) were investigated using ASTER image processing by Testa et al. (2018). El-Desoky et al. (2021) identified the hydrothermal alteration zones in the Arabian–Nubian Shield (a case study of the northwestern Allaqi district, South Eastern Desert, Egypt) using ASTER images. Airborne geophysical studies are advantageous attempts in the reconnaissance and exploration phases, by providing remarkable pieces of information about different natural resources such as mining, oil, geothermal, and environment. Specifically, for mineral occurrence exploration, an airborne magnetometry

---

*Corresponding author.
E-mail address (es): m_lotfi_1014@yahoo.com

survey can delineate promising environments that control the mineralization such as the geological lineaments (faults, contacts, shear zones) and the intrusion-related magmatic units and then, the information extracted from airborne geophysical datasets can be integrated with other regional exploration datasets for Mineral Potential/Prospectivity Mapping (MPM) (Carranza and Sadeghi, 2010; Abedi et al. 2015). Also, in airborne geophysical, edge enhancement techniques are widely used for mapping the geologic features, such as faults, contacts, and dikes (Pham et al. 2021).

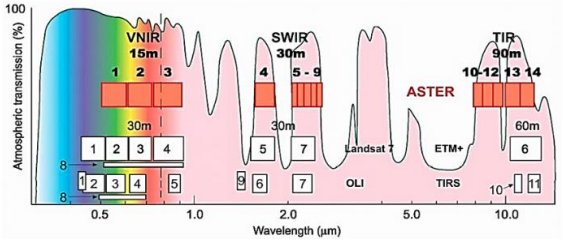

Fig 1. Electromagnetic spectrum comparing ASTER and Landsat (ETM+ and OLI/TIRS) bands (Testa et al. 2018).

The aerial magnetometry on a large scale is useful to determine the location of large fault crushed zones which are often related to mineralization (Kalagari 1992). One of the most important and effective factors in the mineralization of every region is the existence of fractures. Actually, these fractures are a penetration way for mineralizing fluids. Since geology structures like fractures (faults and joints), shear zones, and foliations on the ground surface appear in the aerial and satellite images in the form of lineament (Solomon and Ghebreab 2006), some researchers have used remote sensing and aeromagnetic methods and, field observations along with extraction of structural features specially lineaments to find their tectonic setting (Drury et al. 1994; Arlegui and Soriano 1998; Solomon and Ghebreab 2006; Morelli and Piana 2006). Remote sensing and magnetic data for structural geology investigation in pegmatite areas in the eastern Afghanistan were integrated by Salehi et al. (2015).

Table 1. Comparative of spectral bands and their characteristic features in ASTER, Landsat-7(ETM+) and Landsat-8 (OLI/TIRS) (Testa et al. 2018).

ASTER			Landsat-7 (ETM+)			Landsat-8 (OLI/TIRS)		
Bands	Wavelength (μm	Res. (m)	Bands	Wavelength (μm)	Res. (m)	Bands	Wavelength (μm)	Res. (m)
						1-Ultra blue (coastal/aerosol)	0.435-0.451	30
			1-Visible blue	0.45-0.52	30	2-Visible blue	0.452-0.512	30
1-Visible green/yellow	0.520-0.600	15	2-Visible green	0.52-0.60	30	3-Visible green	0.533-0.590	30
2-Visible red	0.630-0.690	15	3-Visible red	0.63-0.69	30	4-Visible red	0.636-0.673	30
3N-NIR	0.760-0.860	15	4-NIR	0.77-0.90	30	5-NIR	0.851-0.879	30
3B-NIR	0.760-0.860	15						
			8-Panchromatic	0.52-0.90	15	8-Panchromatic	0.503-0.676	15
						9-Cirrus	1.363-1.384	30
4-SWIR	1.600-1.700	30	5-SWIR	1.55-1.75	30	6-SWIR	1.566-1.651	30
5-SWIR	2.145-2.185	30	7-SWIR	2.09-2.35	30	7-SWIR	2.107-2.294	30
6-SWIR	2.185-2.225	30						
7-SWIR	2.235-2.285	30						
8-SWIR	2.295-2.365	30						
9-SWIR	2.360-2.430	30						
10-TIR	8.125-8.475	90						
11-TIR	8.475-8.825	90						
12-TIR	8.925-9.275	90						
13-TIR	10.250-10.950	90	6-TIR	10.40-12.50	30	10-TIR	10.60-11.19	30
14-TIR	10.950-11.650	90				11-TIR	11.50-12.51	30

Res.=Resolution; (30) = Landsat-7 ETM + Band 6 is acquired at 60 m resolution but is resampled to 30 m pixels; Landsat-8 TIRS bands are acquired at 100 m resolution but are resampled to 30 m pixels.

The aim of this paper was to investigate the lineaments and alterations by integrating the different methods of images processing provided by Landsat 7 (ETM+), Landsat 8 (OLI), Terra (ASTER), with aeromagnetic data and finally compare the results with field observations and laboratory tests. Also, the area's aeromagnetic response to different alteration regions by matching aeromagnetic anomalies with alteration zones was investigated.

2. The Study Area and Geological Setting

2.1. Regional Geology

Alborz Mountains are part of the northern margin of the Alpine Himalayan orogenic belt, which is a geological structural zone in the north of Iran (Doroozi et al. 2016) and is located at the site of the closure of the Tethyan basin (Asiabanha and Foden 2012) (Fig 2a). The Alborz magmatic belt has occurred in the hinterland of the Arabian-Eurasia collision plate in the broad Alpine-

Himalayan orogenic belt (Mehrabi et al. 2016). Alborz is part of the Gondwana plate in early Paleozoic (Doroozi et al. 2016). Also, during Ordovician to Silurian, Alborz segregated from Gondwana and finally collided with the Eurasia plate in Triassic (Alavi 1991; Stampfli 1996). The Cenozoic Alborz Magmatic Arc (AMA) is situated in the northern part of Iran with E-W trending which is 600 km long and 100 km wide (Fig 2a).

The magmatic rocks of the Alborz assemblage show a distinct advancement in style, from shallow submarine explosive eruptions to more effusive sub-aerial eruptions (Asiabanha and Foden 2012). The Cenozoic magmatism of the western section of the AMA is named the Alborz-Azerbaijan Magmatic Arc (AAMA), which is separated into two metallogenic zones, Ahar- Arasbaran zone (AAZ) in the north and Tarom-Hashtjin metallogenic province (THMP) in the south (Fig 2a).

The Urumieh-Dokhtar magmatic arc (UDMA) and AAMA are two separate, but parallel, subduction zones that later formed by subduction of the Khoy back-arc basin to the northeast beneath the Alborz-Azerbaijan microcontinent (e.g., Juteau 2003; Azizi and Jahangiri 2008; Aghazadeh et al. 2011). In contrast, other researchers (e.g., Brunet et al. 2003; Ritz et al. 2006; Asiabanha and Foden 2012) proposed the arc magmatism in the AAMA has been caused by a back-arc embryonic oceanic lithosphere during the Late Cretaceous. In the AMA, the Karaj Formation was deposited in central and western AMA in an extensional regime, due to extensive volcanic eruptions in Eocene (Allen et al. 2003; Ballato et al. 2011). The THMP of northwest Iran is hosted by Eocene andesitic basalt lavas (Kouhestani et al. 2017).

This belt (NW-trending) is one of the most important metallogenic provinces of Iran that hosted by mineralization of porphyry-epithermal deposits with Eocene to Oligocene volcanic and plutonic events.

2.1. Local Geology and Mineralization

Rashid-Abad (Rasht Abad) area is located approximately 45 km north of Zanjan, in NW Iran. The present study area is located on a part of the geological map of Hashtjin (Faridi and Anvari 1996) at 1:100000 scale, between the longitudes 48° 21' 6.001" to 48° 23' 53.999"E and the latitudes 37° 04' 43" to 37° 07' 26"N (Fig 2b).

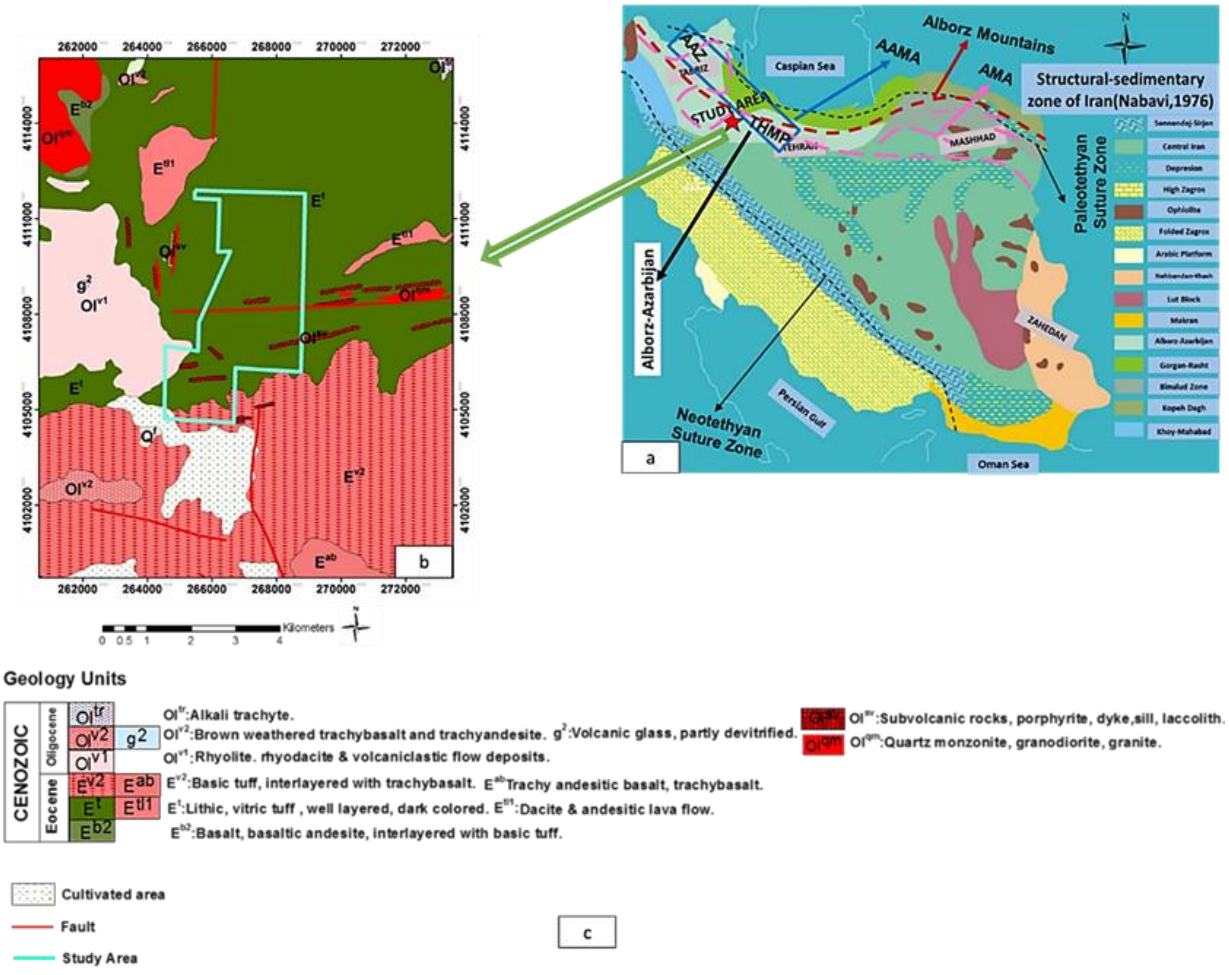

Fig 2. (a) Location of the study area on the map of structural-sedimentary zones of Iran (Nabavi 1976). (b) Geological map of Hashtjin at 1:100000 scale. (c) Legend for map (b).

According to Nabavi (1976), this area is situated in the Alborz (western)-Azerbijan zone (Fig 2a). Generally, the stratigraphy of the study area is based on the geological map of Hashtjin related to Eocene and post-Eocene periods. The main units of the study area include; (Et): lithic-vitric tuff, well layered and dark-colored. (EV2): basic tuff, interlayered with trachybasalt. (Olv1): rhyolite and rhyodacite-volcaniclastic flow deposits. (Olsv): subvolcanic rocks, porphyrite, dike, sill, and laccolith (Fig 2b, c). Rashid-Abad exploratory area is a tectonically active region. Figure 3 shows the distribution of faults in the study area (Faridi and Anvari 1996).

In the study area there is an east- west trending fault, which led to displacement in rock units, which is called Rasht-Abad fault.

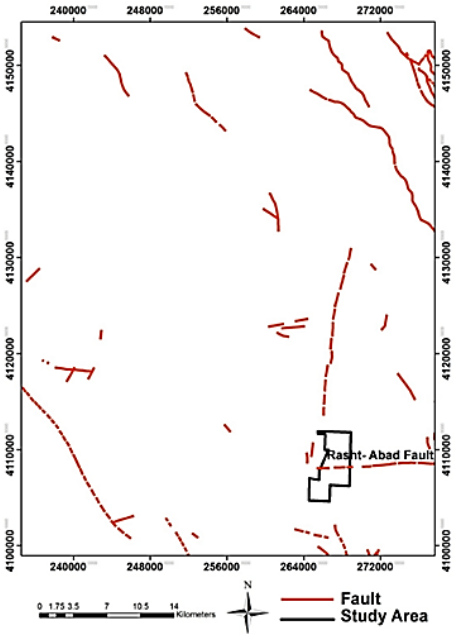

Fig 3. Location of faults in geological map of Hashtjin at 1:100000 scale.

The main mineralization vein comprises silica-breccia. In this area, the main siliceous-brecciaed vein consists of tuffs, andesitic tuffs, andesite, dacite, rhyolite, trachyandesite, basaltic trachyandesite, and basalt. There is probably hydrothermal mineralization in this region, because hydrothermal veins that have been silicated are abundant, which proves this claim. Mineralization has occurred along these veins (Fig 4a). Two mineralization stages have been formed in the study area: (1) the hypogene stage consists of magnetite (oxide phase), chalcopyrite, and burnite (sulfide phase); (2) the Supergene stage consists of hematite and goethite (oxide phase), covelit (sulfide phase), and azurite, malachite, and calcantite of copper carbonates. Since key mineralized zones are accumulated with phyllic, silicic, propylitic, argillic, and iron oxide alterations, the target mineralization in this research is investigation of alteration zones related to Cu and Fe mineralization in this area (Fig 4).

3. Data and Methods

In this area, the lineaments and alterations have been investigated using the following items: (1) the satellite images of Landsat 7(ETM+) and Landsat 8 (OLI) with the scene number-167/034 (Path/Row); (2) ASTER satellite image with the scene number- ASTER IB-070302-372; (3) aeromagnetic data of Hashtjin at 1:100000 scale. These actions have been performed with ER Mapper 2013©, ENVI- 5.0©, Oasis Montaj 7.2.1©, and Arc GIS 10.7.1© software packages. Eventually, in order to validate the performed studies, the results have been evaluated by field observations and laboratory investigations. The used data, methods, and different methods of interpretation introduced in the study area have been presented in the given flowchart (Fig 5). Also, each of the methods and their interpretations is described in detail below.

3.1. Remote Sensing Data

Due to the presence of the radiometric and geometric errors, satellite images require correction before processing. To achieve this, radiometric correction of Landsat 7 ETM+ and Landsat 8 OLI images was performed using ER Mapper 2013© software. Moreover, using methods of the dark subtract and internal average relative reflectance in ENVI 5.0© software, the radiometric correction was applied to the ASTER satellite image. Also, the geometric correction of all satellite images was done by the coordinate system (UTM-Zone 40 North, Datum GS- 84) in Arc GIS 10.7.1© software.

3.1.1. ETM+ and OLI

3.1.1.1. Band Ratio (BR) Method

Band ratio (BR) is a well-established method to identify and map the alteration zones (e.g., Dehnavi et al. 2010; El Khidir and Babikir 2013; Sadiya et al. 2014; Fakhari et al. 2019; Mehdikhani and Imamalipour 2021). This technique enhances the contrast between features by dividing digital number (DNsa) values at peaks and troughs in a spectral reflectance curve (Sabins 1997). In addition, this method is created to display the spectral contrast of specific absorption features, and reduce sun light, topography effects, and also for illustrating data of images spectral has been widely applied in geological remote sensing (Rowan et al. 2006).

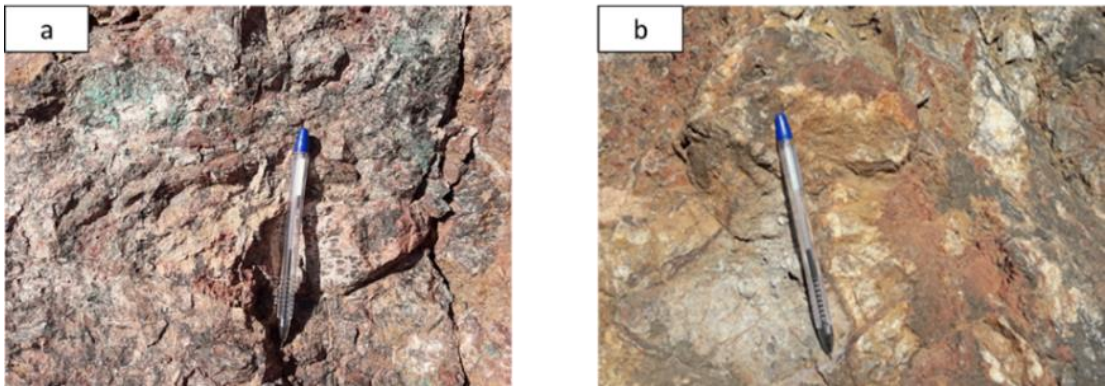

Fig 4. (a) Copper mineralization in siliceous-brecciaed vein in the study area. (b) Iron Oxide mineralization in the study area.

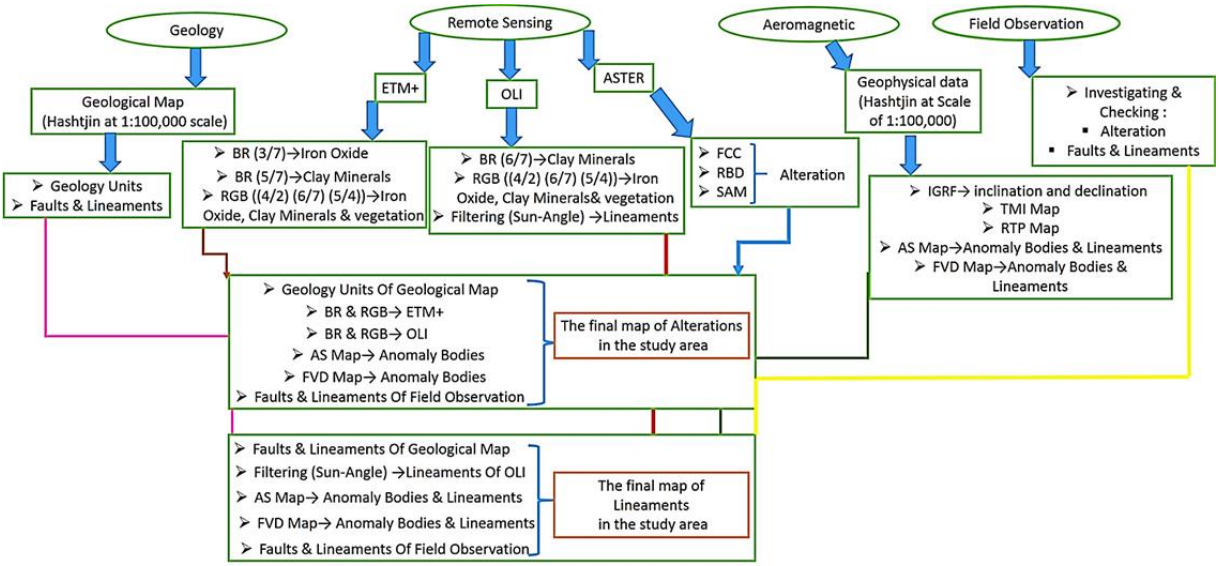

Fig 5. (a) Flowchart of data, methods and different methods of interpretation introduced in the study area.

There are various band ratios that are used to enhance the particular feature, e.g., band ratios 3/1, 5/7, 4/3, 4/2, 5/4, and 6/7 to identify the hydrothermally altered rocks and iron alteration zones (Sabins 1997; Sabins 1999) in the study area. The Landsat 7 ETM+ band ratio 3/1 effectively enhances iron alteration as iron minerals such as goethite and hematite, which have maximum reflectance within band 3 (0.63-0.69 µm) and minimum reflectance within band 1 (0.45-0.52 µm), (Sabins 1997). Similarly, band ratio 5/7 separates altered clay minerals from an unaltered rock. This band ratio is used for detecting high values of hydroxyl-bearing (OH-bearing minerals (kaolinite, epidotes, chlorites, etc.) (e.g., Sabins 1997; Sabins 1999; Marc and Rowan 2010, etc.). The band ratios described above was applied to ETM+ data of the study area (Fig 6, 7).

Also, a color composite image was created using a band ratio combination of RGB (3/1, 5/7, 4/3) to determine the placement of hydrothermally altered rocks. Therefore, the areas which are pinkish to violet color are hydrothermally altered zones, while iron-oxides and vegetation appear in blue and yellow, respectively (Fig 9a). In Landsat 8 OLI, band ratios 4/2, 6/7, and 5/4 are respectively equivalent to band ratios 3/1, 5/7, and 4/3 in Landsat 7 ETM+. Therefore, band ratio 6/7 separated altered clay minerals from unaltered rocks in the study area (Fig 8).

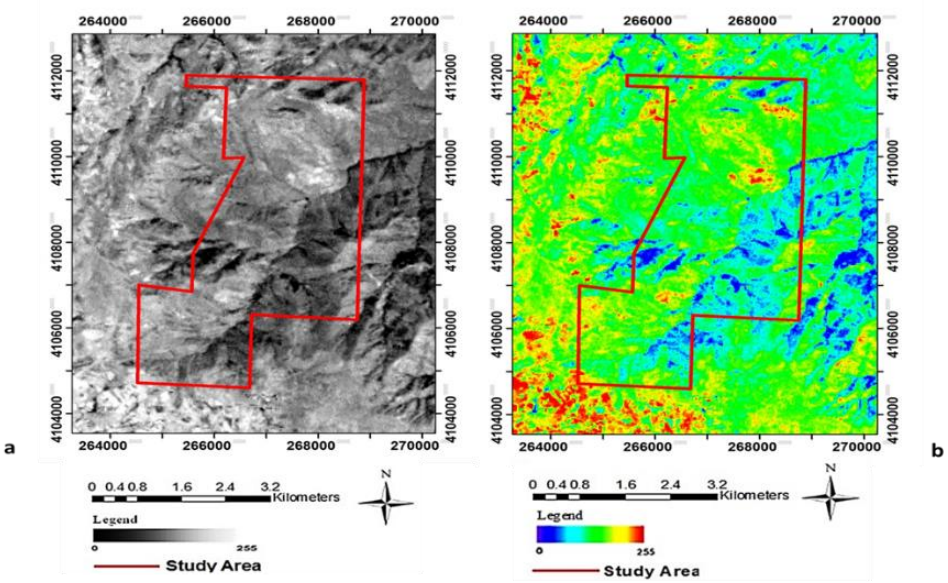

Fig 6. Landsat 7 ETM+ band ratio 3/1. (a) Grayscale image. (b) Colored image.

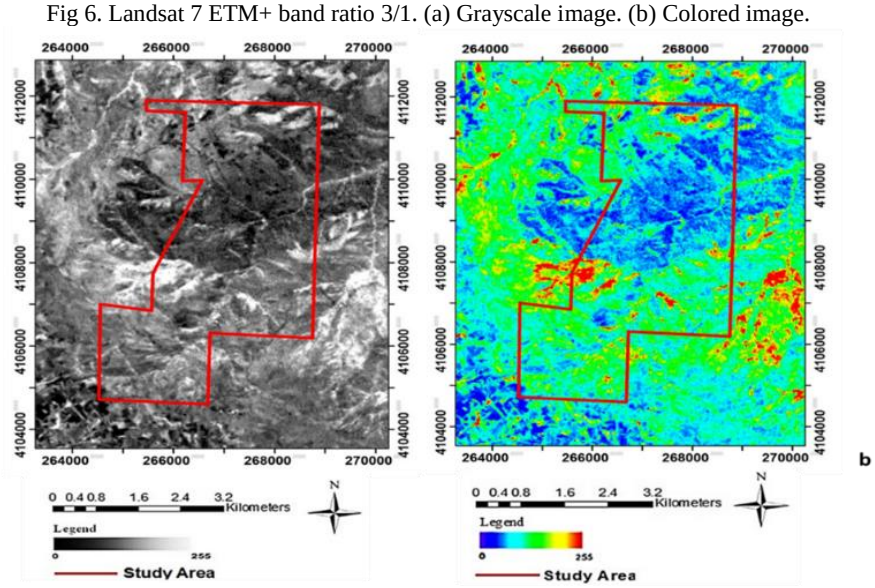

Fig 7. Landsat 7 ETM+ band ratio 5/7. (a) Grayscale image. (b) Colored image.

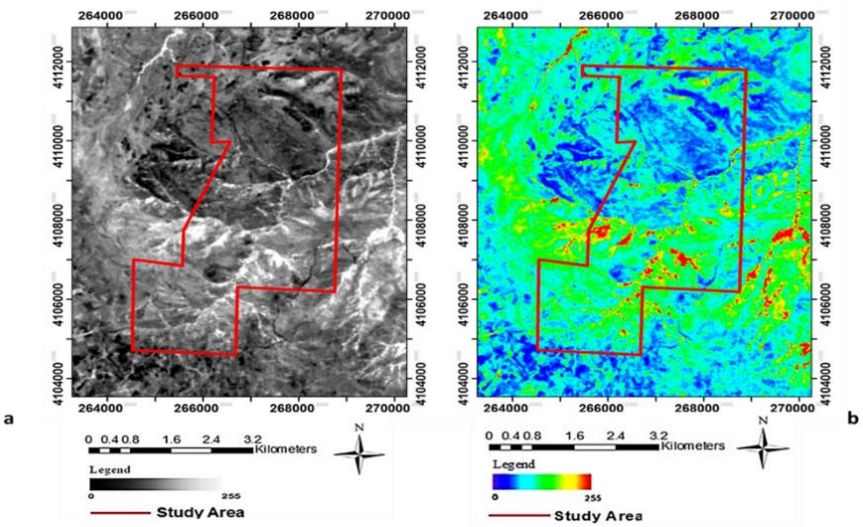

Fig 8. Landsat 8 OLI band ratio 6/7. (a) Grayscale image. (b) Colored image.

Also, the combination of band ratios 4/2, 6/7, and 5/4 in RGB image was used which the band ratio 4/2 enhanced iron oxide alterations in blue color, band ratio 6/7 separated the altered clay minerals in pinkish to violet color, and band ratio 5/4 showed vegetation in yellow color (Fig 9b). The results of band ratio combinations in RGB for both Landsat-7 and 8 seem to be similar in their ability to target hydrothermal alteration mapping. Here it should be noted that along with all grayscale images, a colored image is also used, which the red color in these images is the most similar to the mentioned phenomena.

3.1.1.2. Filtering Method

One of the most useful techniques to enhance the lineaments is using various filters. In this part, to enhance the sharp edges such as lineaments and faults in the special direction, utilizing a sun-angle filter of OLI data in ER Mapper 2013© software was applied. This filter was used to the grayscale image of band 8 (panchromatic band) of Landsat 8. The reason for selecting this band is the highest spatial resolution (15 meters) of this band comparing to other bands.

For this purpose, by applying the sun-angle filter in three radiation directions of N-S, SW, and SE, the lineaments with the E-W, NW-SE, and NE-SW trends were enhanced respectively in study area. Also, the most important lineament with the East-West trend was called Rasht-Abad fault (Fig 10a-c).

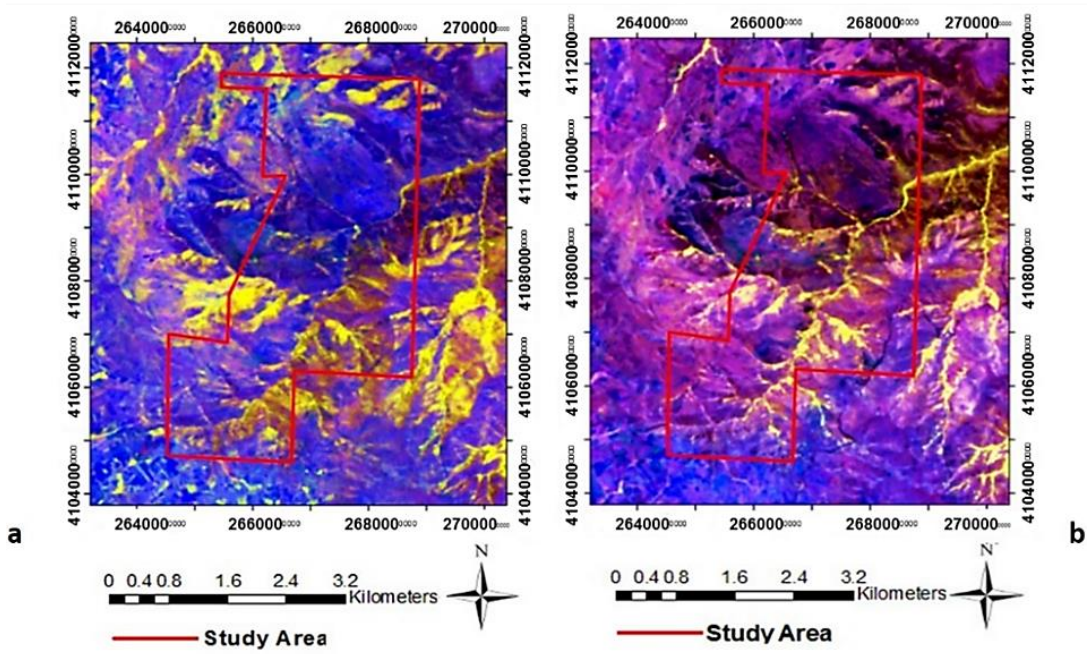

Fig 9. (a) Landsat 7 ETM+ color composite of bands ratio (3/1, 5/7, 4/3) in RGB, respectively. (b) Landsat 8 OLI color composite of bands ratio (4/2, 6/7, 5/4) in RGB, respectively.

3.2. Processing and Interpretation of ASTER Satellite Images

Since the ASTER sensor was designed based on geologic needs, therefor images of this sensor can be used as a powerful tool in the exploration of the mineral resources in the early phases for the preliminary mineralogy and alteration maps at a low cost and high accuracy. ASTER satellite data with a better spectral resolution (more bands) is more able to separate the alteration zones comparing to Landsat 7 and Landsat 8 satellite data. In this study, false-color composite (FCC), relative absorption band-depth (RBD) and spectral angle mapper (SAM) have been applied in the enhancement and investigation of the alterations.

F.C.C (R=4 G=6 B=8) is one of the most suitable color combinations to identify the alteration areas in the most of the deposits and it was also used in the study area (Fig 11). In this color composite, the minerals related to the propylitic zone (epidote, chlorite) are seen as green and the argillic zone (clay minerals) is seen as pink. This issue is caused by the high reflection of alunite, kaolinite, and muscovite (sericite) minerals in band 4 in relation to bands 6 and 8 (e.g., Testa et al. 2018). By applying the F.C.C method in the study area, argillic alteration is the highest in the western, eastern and central parts respectively and propylitic alteration in the southeast part has appeared.

3.2.2. Relative Absorption Band Depth (RBD)

RBD is one of the methods of image processing aiming to determine and separate the alteration areas which is achieved by dividing the sum of the highest reflection to the highest absorption. For each absorption feature, the numerator is the sum of the bands representing the shoulders, and the denominator is the band located nearest the absorption feature minimum (Fig 12) (Crowley et al. 1989).

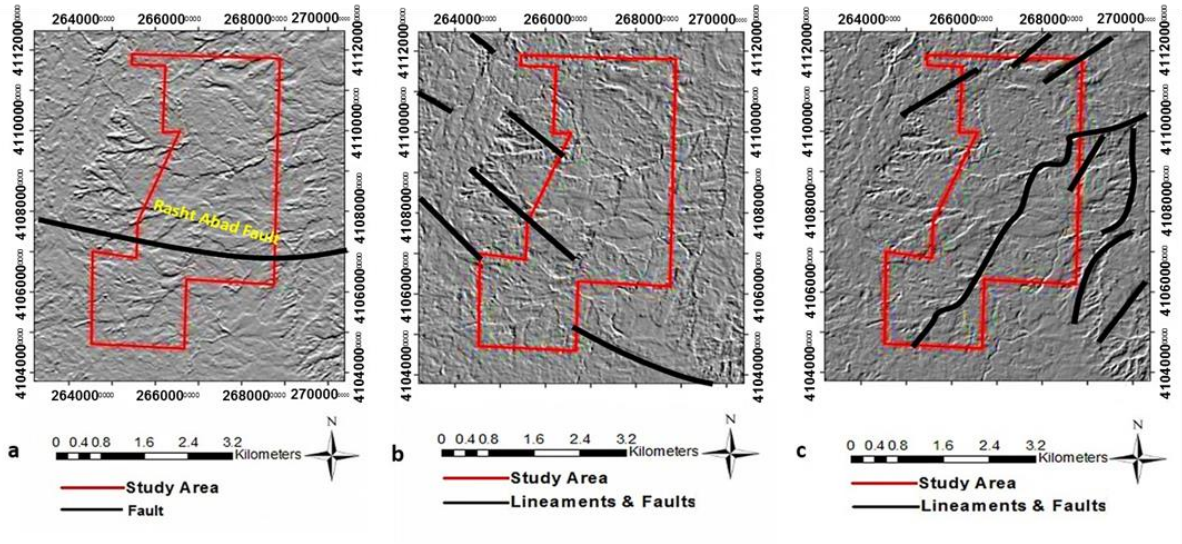

Fig 10. OLI panchromatic band image after the use of Sun angle filter. (a) Enhancement of E-W lineaments. (b) Enhancement of NW-SE lineaments. (c) Enhancement of NE-SW lineaments.

Table 2. Types of band ratios and alterations that were used to create the maps of phyllic, argillic and propylitic alteration zones in the study area.

Minerals	Band Ratio (RBD)	Alteration Type	Reference
Illite/Sericite-Muscovite/Quartz	RBD6: (5+7)/6	Phyllic	Rowan (USGS)
Alunite/Kaolinite/Montmorillonite	RBD5: (4+6)/5	Argillic	Rowan (USGS)
Epidote/Chlorite/Calcite	RBD8: (7+9)/8	Propylitic	Rowan

Alteration zones are identified based on the relations derived from spectral features of their component. Each alteration has its special band combination. In the SWIR range of ASTER sensor, the bands 5, 6 and 8 are related to the absorption of certain minerals which these alterations and their main minerals and related band ratio are shown in Table 2. By using the RBD technique in the study area, the band ratios of any kind of alteration appeared as light color in grayscale images and as red color in colored images.

3.2.2.1. Phyllic Alteration (RBD6)

This zone is characterized by the main minerals of illite, muscovite (sericite) and quartz. These are minerals with the highest absorption depth at 2.20 µm (Fig 13a) that coincide with band 6 of ASTER image (Li et al. 2014). In the study area (Fig 13b, c), phyllic zone has been enhanced from the center to the east, west, and south parts of the region.

3.2.2.2. Argillic Alteration (RBD5)

This zone is included the main minerals of kaolinite, montmorillonite, and alunite. These are minerals with the highest absorption depth at 2.17µm (Fig 14a) that coincide with band 5 of ASTER image (Li et al. 2014). In Figure 14b, c argillic zone in the west, southwest, and north of the study area, as well as outside the study area in the northwest, north, and southeast of the area has been enhanced.

3.2.2.3. Propylitic Alteration (RBD8)

This zone is indexed with the main minerals of epidote, chlorite, and calcite. These minerals have the highest absorption depth at 2.33 µm (Fig 15a) and are matched with band 8 of ASTER image (Li et al. 2014). In the study area (Fig 15b, c), the propylitic zone has been enhanced in the western part of the region. It has also appeared outside the study area in the western and southeastern parts.

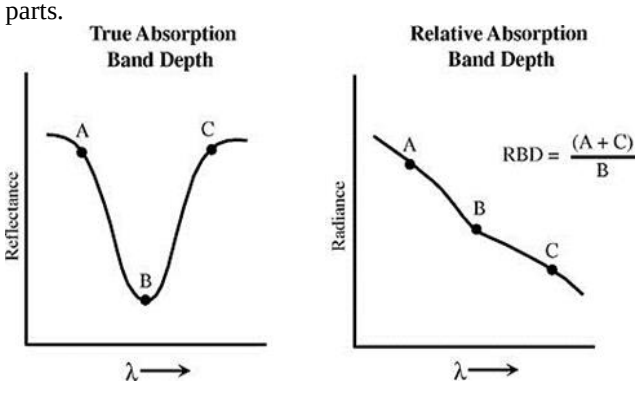

Fig 12. Relative Band Depth (RBD) ratio schematic (modified from Crowley et al. 1989).

3.2.3. Spectral Angle Mapper (SAM)

The spectral angle mapper (SAM) algorithm assumes that a pixel of remote sensing images shows certain ground cover material, which can be uniquely assigned to only one ground cover class. The spectral similarity between two spectra is measured by calculating the angle between the two spectra considering them as vectors in a space with equal dimensionality to the number of bands (Rashmi et al. 2014).

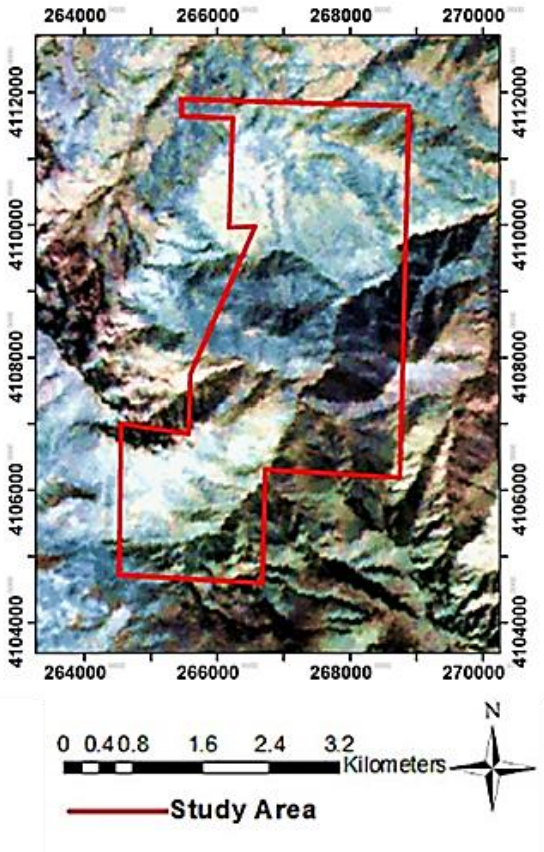

Fig 11. False Color Composite (F.C.C) in RGB mode (R = 4 G = 6 B = 8).

The SAM is a physically-based spectral classification. The algorithm of this method calculates the similarity between the image spectrum and a reference spectrum (such as USGS spectral library). The SAM compares the angle between the endmember spectrum vector and each pixel vector in an n-dimensional space, (n is the number of spectral bands), (Kruse et al. 1993). The spectral angle can have values between 0 andπ2.

To achieve this, initially an image with the color combination of 468 (RGB) was created. Because in this study, our aim was to investigate the argillic and propylitic alterations which the spectrums related to the main minerals of argillic and propylitic zones were achieved by the ENVI 5.0© software (Fig 16a). Finally, the argillic and propylitic alterations map was prepared. Argillic alteration was slightly enhanced in the western part of the study area, as well as, outside the study area in the eastern, southern and northwestern parts which was displayed a relative increase, respectively. Also, propylitic alteration was enhanced in the northern, central and a little in the southern parts, respectively. In this area, the results were investigated from different several angles. Finally, the best amount of angle which is 0.1 was calculated and applied using the ENVI 5.0© software (Fig 16a, b).

3.3. Preprocessing of the Aeromagnetic Data

The source of aeromagnetic data in the study area, was aerial geophysical data (Hashtjin at Scale of 1:100,000) with a 7.5 km line spacing, that was supervised by the Geological Survey of Iran (GSI). One of the preprocessing phases of aeromagnetic data is using the IGRF (International Geomagnetic Reference Field) or the regional correction.

IGRF was introduced by the International Association of Geomagnetism and Aeronomy (IAGA). Also, it has been produced and updated under the direction of IAGA since 1965. In the study area, initial correction was already applied to the initial data of this region by the GSI's monitoring team. In this paper, based on the model IGRF, IGRF parameters used to compute the values for the geomagnetic field, are as inclination and declination of 54.67◦ and 3.73◦ in the study area, respectively.

These parameters are used to calculate the reduced to pole (RTP) map and subtract the earth's magnetic main field.

3.4. Processing of the Aeromagnetic Data

3.4.1. Investigation of the Total Magnetic Intensity (TMI) Map

The total Magnetic Intensity (TMI) map is the basis of the magnetic data which shows the total intensity of the earth's magnetic field in different measuring points. The TMI data forms the basis for better application of enhancement filters needed for detailed structural interpretation of the study area (Okoro et al. 2021). Maximum and minimum field intensity in the study area is 39646 and 39371 nanotesla (nT), respectively. Generally, in the total magnetic field intensity map, a positive anomaly in the western of the area is observed. The trend of increasing magnetic field intensity begins from the west and southwest, and reduces towards the northeast (Fig 17a). The identification of anomalies is not accurately possible on the map, so by applying different filters on it in the next phases, magnetic data is investigated and interpreted.

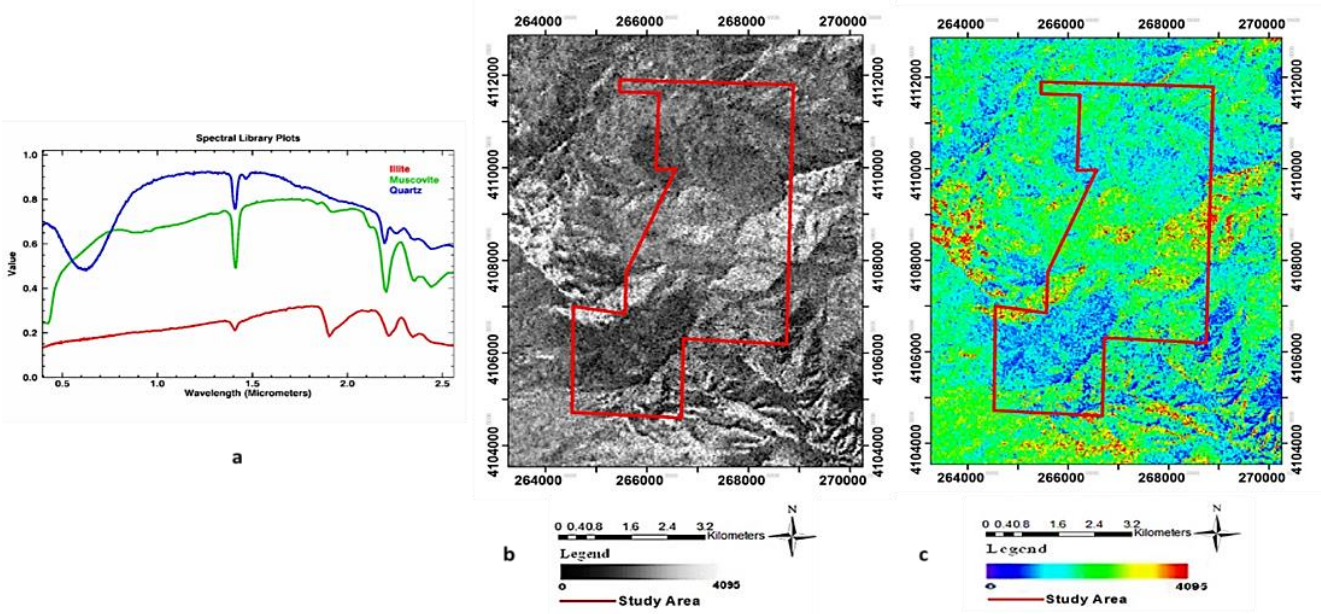

Fig 13. (a) Spectrum related to the highest absorption of the main minerals of phyllic zone in ASTER image. (b,c) Phyllic alteration from RBD6. (b) Grayscale image. (c) Colored image.

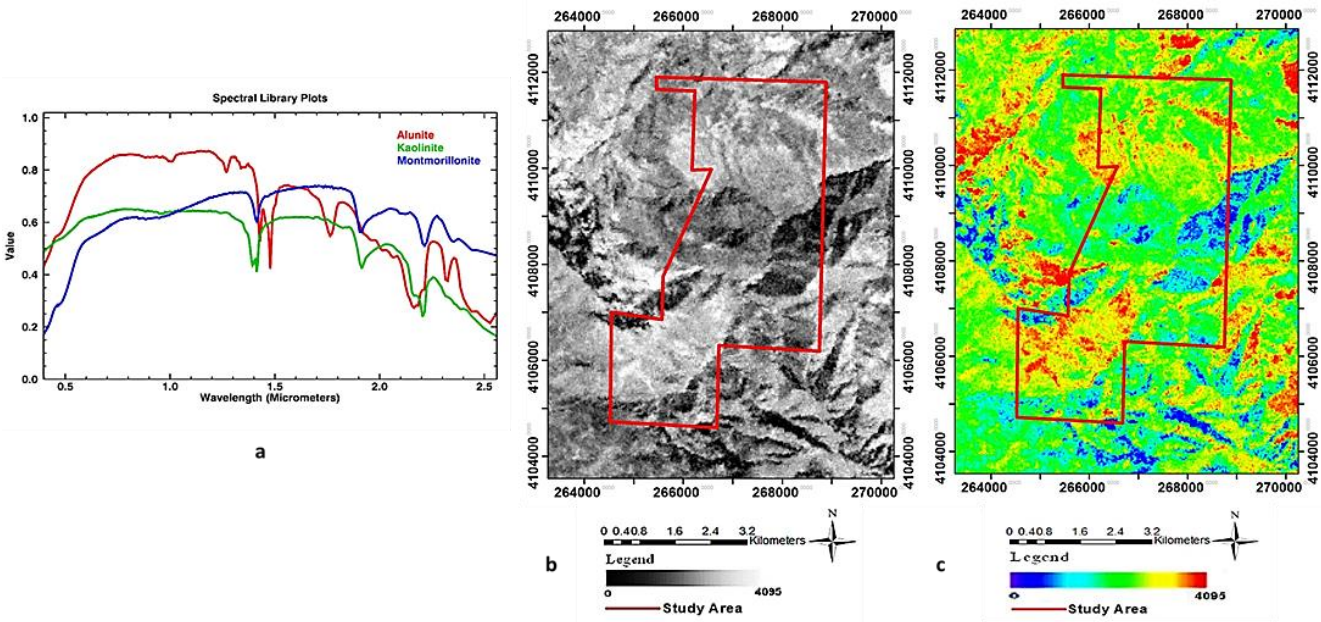

Fig 14. (a) Spectrum related to the highest absorption of the main minerals of zone in argillic ASTER image. (b,c) Argillic alteration from RBD5. (b) Grayscale image. (c) Colored image.

3.4.2. Investigation of the Reduction to the Pole (RTP) Filter

The reduced-to-pole (RTP) transformation is used to set the Earth's magnetic field inclination along the magnetic pole giving rise to positioning a positive pole over causative magmatic sources (Ghaeminejad et al. 2020). The RTP produces a symmetric pattern of the magnetic signal, which facilitate the interpretation of the magnetic anomalies (Abedi and Oskooi 2015). The first step in the interpretation of the magnetic data is eliminating the dipole effect of the magnetic field. According to the angles of magnetic declination and inclination of the earth, it is obvious that the source of these anomalies does not exactly place below measuring points and their form may also change slightly. Therefore, in order to delete translocation, the RTP filter is applied. Using this filter, an observed TMI anomaly is transformed into an anomaly that would be measured at the north magnetic pole (Li 2008). The angles of magnetic declination and inclination in the study area are 54.67 and 3.73 degrees, respectively. In regard to the previous descriptions in section 3-4-1, the main location of the anomaly with high magnetic intensity has been moved from the west to the northwest in the area (Fig 17b).

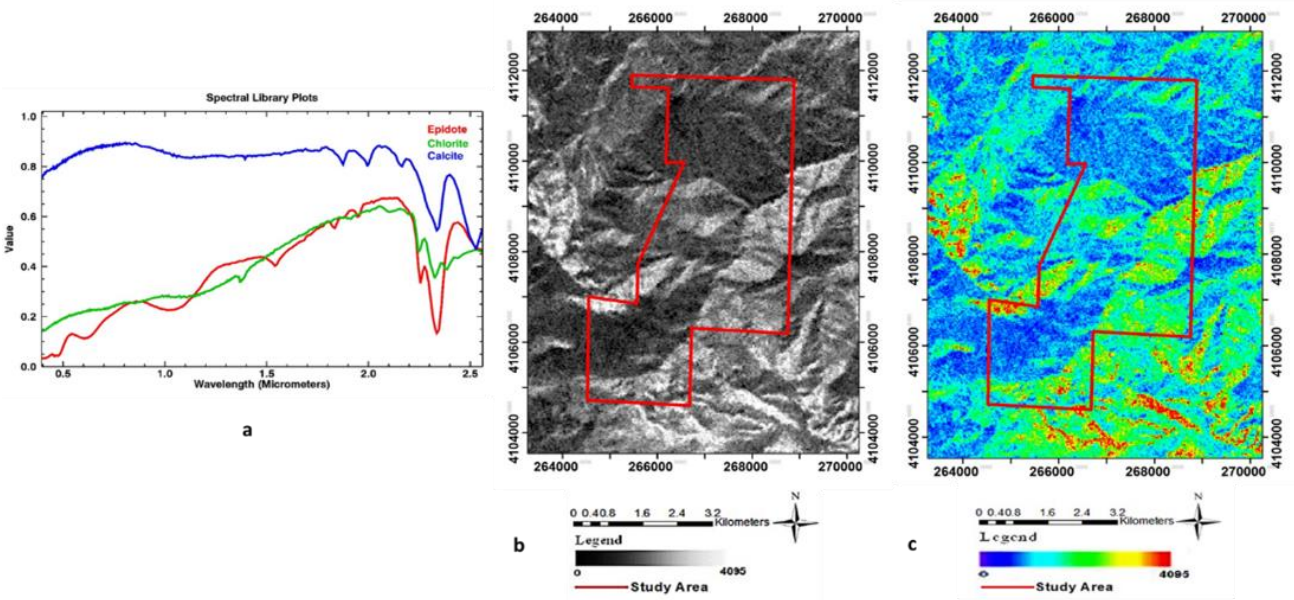

Fig 15. (a) The spectrum related to the highest amount of absorption of the main minerals of propylitic zone in the ASTER image. (b,c) Propylitic alteration from RBD8. (b) Grayscale image. (c) Colored image.

3.4.3. Investigation of the Analytic Signal (AS) Filter

Using the analytic signal method to determine anomaly parameters of the magnetic field was developed first by Nabighian in 1972. Generally, one of the features of the analytic signal filter is its use in identification of anomaly boundaries, magnetic lineaments, and hidden and obvious fault (Nabighian 1972; Roest and Pilkington 1993). Nabighian (1972) indicated that the 2D ASA (analytic signal amplitude) of a magnetic anomaly profile can be given by (Eq.1):

$$|ASA(x)| = (V^2x+V^2z)^{1/2} \quad (1)$$

Where Vx and Vz are the horizontal and vertical derivatives of the magnetic anomalies, respectively. In addition, 2D ASA of some idealized causative body geometries can be approximated by the following generalized equation (Eq.2) (Nabighian 1972, Thurston and Smith 1997, Salem et al. 2004, Salem 2005).

$$|ASA(x)| = A/[(x-x_o)^2+z_o^2]^q \quad (2)$$

Where A is the amplitude coefficient related to the physical properties of the source, q is the shape factor related to the geometry of the source, xo and zo denote the exact origin and depth to the top of the causative body, respectively. Salem et al. (2004) related the shape factor, q and the structural index, N (Thompson 1982) for different source geometries by the equation $N = 2q - 1$. Therefore, the structural indexes of 0, 1 and 2 for magnetic anomalies over a contact, a thin dike and a horizontal cylinder that with shape factors as 0.5, 1, and 1.5 are corresponded, respectively (Srivastava and Agarwal 2010). The AS is the combination of vertical and horizontal gradients. It estimates the source characteristics based on the calculation of the first derivative of magnetic anomalies. Also, it is a filter applied to magnetic data and is aimed to simplify the fact that magnetic bodies usually have a positive and negative peak associated with them, which in many cases make it difficult to determine the exact location of the causative body (Lawal et al. 2021).

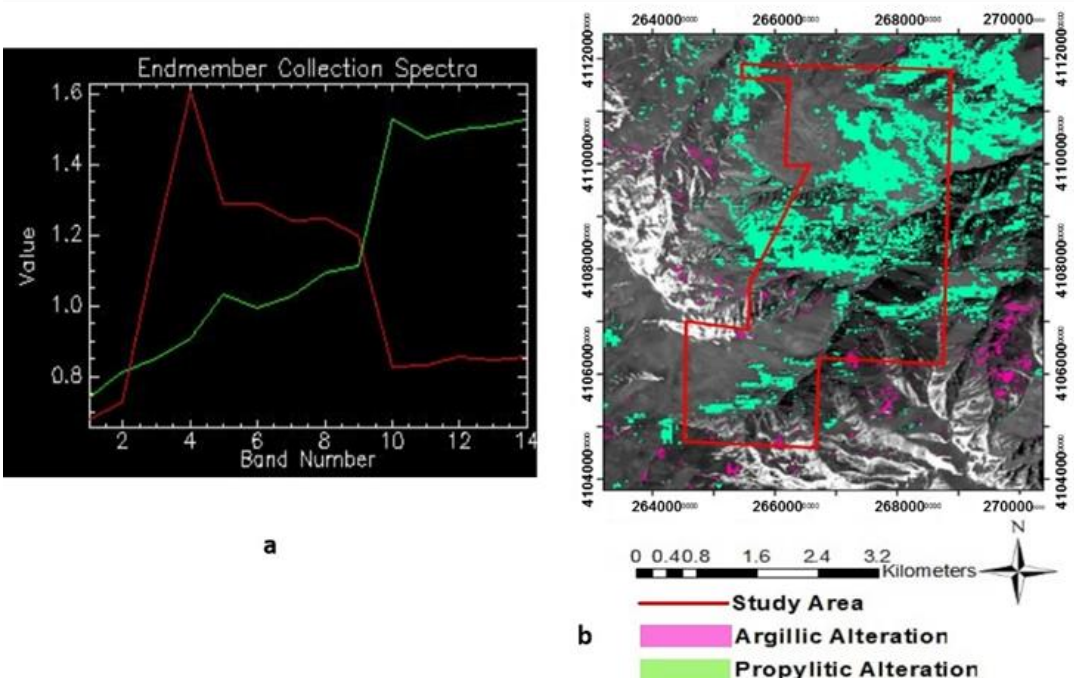

Fig 16. (a) Spectrum related to the main minerals of argillic and propylitic zones in ASTER color composition RGB, 468. (b) Argillic and propylitic alterations with SAM method

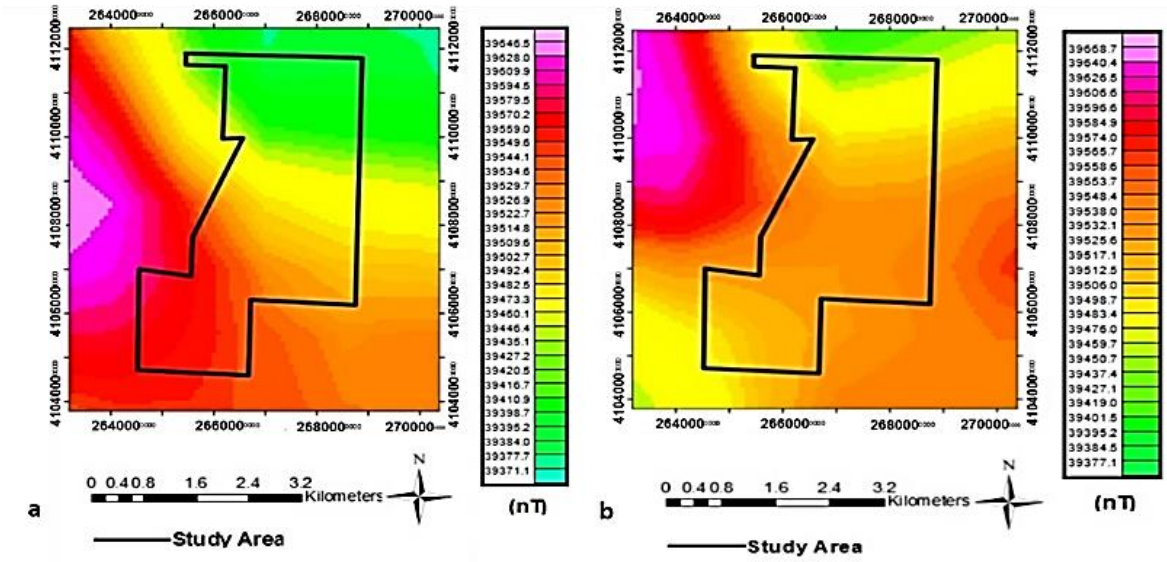

Fig 17. (a) Total magnetic field intensity map (TMI). (b) Reduction to the pole map (RTP).

The analytic signal technique was used in this study to define the edges of magnetic anomalies. In the AS derivative map, (Fig 18a) the variation in the magnetization of the magnetic sources, discontinuities, and anomalies were highlighted in the study area. Also, the boundaries of two huge anomalies, one in the northwest with the extension from the NW to the SE and the other one with a more distant and outside the location of the study area (east of the area) with an approximately northern trend from the NE to the SW, were appeared. Between these two anomalies, less magnetic field intensity was observed, which may be due to the existence of a lineament with an E-W trend, which is most likely the same as the Rasht-Abad fault. In the boundary of huge anomaly (NW) with the extension from the NW to the SE, there was a linear and narrow area with high magnetism (violet color) with the same as the extension, which the magnetic field intensity is higher than other parts of the area. This may indicate significant mineralization caused by the presence of intrusive bodies

and the penetration of hydrothermal fluids in fractures and faults in the region. Moreover, there were the boundaries of anomalies with blue color in the north and south of the study area that show the lowest magnetic field intensity compared to other parts of the area.

These anomalies were recognized as negative anomalies. In addition to the magnetic anomaly investigations, the lineaments related to these anomalies and other lineaments were extracted using the analytic signal method in this study. (Fig 18a).

3.4.4. Investigation of the First-Order Vertical Derivative (FVD) Filter

Generally, Differentiation is used to investigate the changes of magnetic field intensity in different directions. Derivative filtering methods are used to sharpen the edges of magnetic anomalies and better locate their positions (Jayeoba et al. 2015).

To enhance shallow anomalies against deeper sources, a filter called first-order derivation (FVD) is used in the vertical direction. Also, the FVD is normally applied to the aeromagnetic data to accentuate near-surface structural features and shallow sources generating magnetic anomalies (Salawu 2021; Okoro 2021). The rate of change of magnetic signal in the vertical direction is calculated by FVD method. The FVD method highlights the lineament and anomalies due to their short wavelength feature (Jayeoba et al. 2015; Okoro 2021).

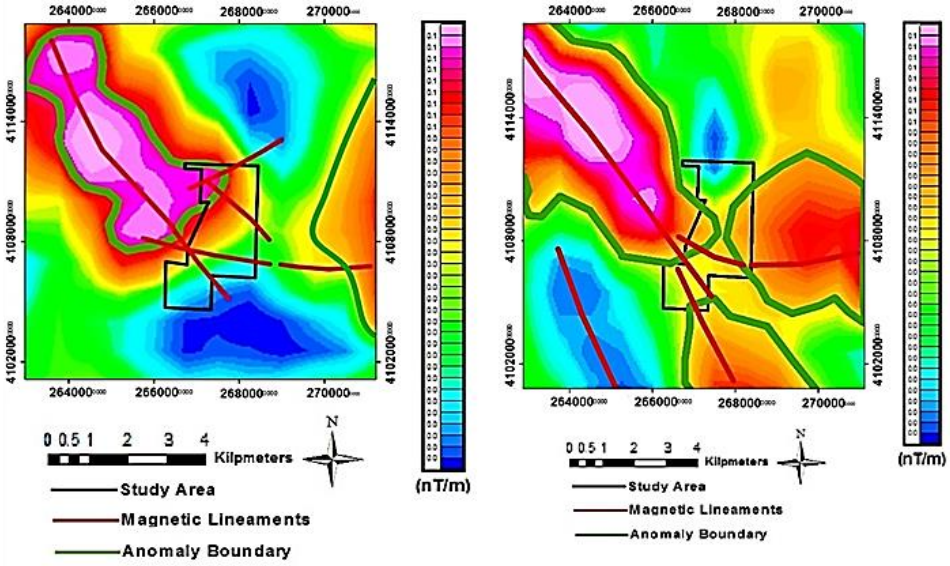

Fig 18. (a) Analytic Signal (AS) filter. (b) First-order Vertical Derivative (FVD) filter.

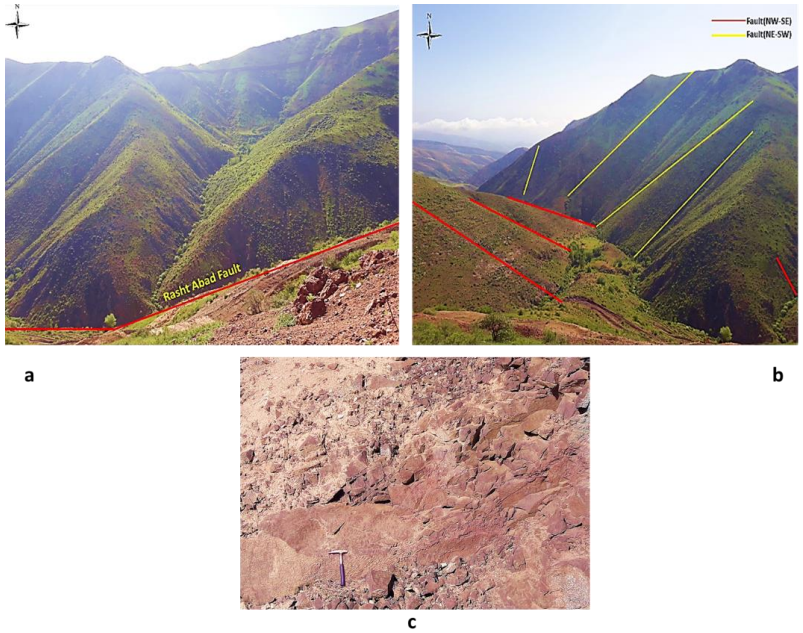

Fig 19. (a) A view of the Rasht-Abad fault (View to the north). (b) A view of faults with NW-SE and NE-SW trends (View to the north). (c) A view of Crushed tuffs.

Mathematically, the first vertical derivative is given by the equation. The FVD method with respect to depth (z) is given in Eq. (3) as (Evjen 1936):

$$FVD=-\frac{\partial F}{\partial Z} \quad (3)$$

Where F is the detected RTP aeromagnetic anomaly field, much insight into shallow subsurface structural features is obtained from the visual investigation of prominent magnetic signatures on FVD map (Salawu 2021). The FVD transformation enhances near-surface structural features (Salawu 2021). Generally, one of the features of the first-order-derivation, such as the analytic signal filter is the identification of anomaly boundaries, magnetic lineaments, and hidden and obvious faults. In the study area, the boundary of three huge anomalies was appeared: (1) the first in the NW; (2) the second in the south of the area, which both had the NW-SE trend; (3) the third anomaly was in the east of the area with an almost eastern-western trend. In Figure 18b, same as the analytic signal (Fig 18a), there was a linear and narrow area with high magnetism (violet color) and with the NW-SE trend in the northwest anomaly. It can be due to the presence of intrusive bodies and the penetration of hydrothermally fluids in fractures and faults in the region, which is created significant mineralization compared to other regions. In addition to the three major anomalies, there were two weak anomalies (blue color) in the southwest and north of the study area, which one of the two anomalies was located parallel to anomaly 2 and had an NW-SE trend. These anomalies were identified as negative anomalies. Finally, the lineaments related to anomalies and as well as other possible lineaments were accentuated in the study area (Fig 18b).

4. Result and Discussion

4.1. Result of Interpretation of ETM+&OLI

Using the Iron-oxide band ratio method (3/1) in ETM+ was led to the enhancement of the iron-oxides in the western and northern parts of the study area, while its amount inside the study area was relatively lower than outside. Therefor in the southwest and northwest parts was increased respectively (Fig 6). The band ratios 5/7 and 6/7 were used in the ETM+ and OLI images respectively, to highlight hydrothermally altered rocks, which the results of both images were close to each other and appeared in the central and western parts of the area. Moreover, they were indicated an enhancement outside of the study area, the southeast of the region (Fig 7, 8). Also, the band ratio combination of (R=3/1 G=5/7 B=4/3) and (R=4/2 G=5/4 B=6/7) in the ETM+ and OLI images used to separate vegetation in yellow color, clay minerals in pinkish to violet color, and iron oxide alteration in blue color. Actually, altered areas were enhanced in some parts of the west, south, and to a small extent in the northeast (Fig 9a, b). The result of band ratio (R=4/2 G=5/4 B=6/7) in OLI compared to ETM+ (R=3/1 G=5/7 B=4/3) due to masking out vegetation, was more widely used and interpreted in this area (Fig 9b). Altogether, the results of band ratio combinations in RGB for both Landsat-7 and 8 seem to be similar in their ability to target hydrothermal alteration mapping.

4.2. Result of Interpretation of ASTER

Using the Iron-oxide band ratio method (3/1) in ETM+ was led to the enhancement of the iron-oxides in the western and northern parts of the study area, while its amount inside the study area was relatively lower than outside. Therefor in the southwest and northwest parts was increased respectively (Fig 6). The band ratios 5/7 and 6/7 were used in the ETM+ and OLI images respectively, to highlight hydrothermally altered rocks, which the results of both images were close to each other and appeared in the central and western parts of the area. Moreover, they were indicated an enhancement outside of the study area, the southeast of the region (Fig 7, 8). Also, the band ratio combination of (R=3/1 G=5/7 B=4/3) and (R=4/2 G=5/4 B=6/7) in the ETM+ and OLI images used to separate vegetation in yellow color, clay minerals in pinkish to violet color, and iron oxide alteration in blue color.

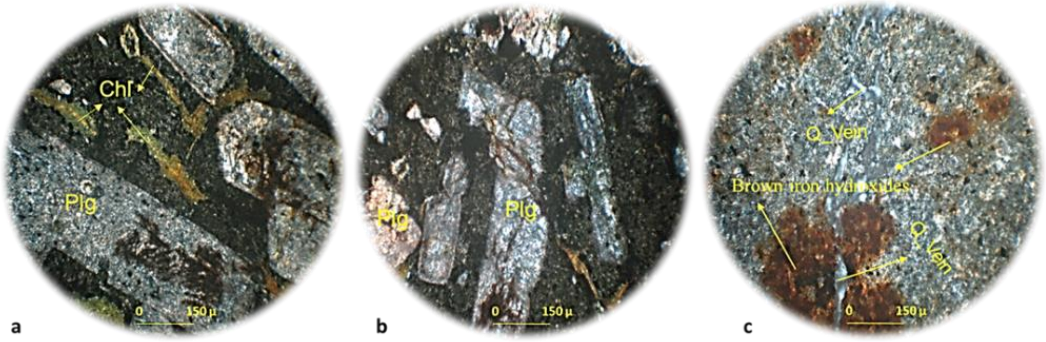

Fig 20. Photomicrographs of representative rock types: (a) A view of the sericite and argillic plagioclase (Plg) coarse crystals with traces of chloritization (Chl) in the context of rock (XPL). (b) A view of the rock context and plagioclase coarse crystals which have been crushed and mylonitized, which have been surrounded by argillic materials impregnated with iron-hydroxides. (c) A View of argillic vitroclastic tuff that has been cut by quartz veins and has left behind traces of brown iron hydroxides in the fractures path.

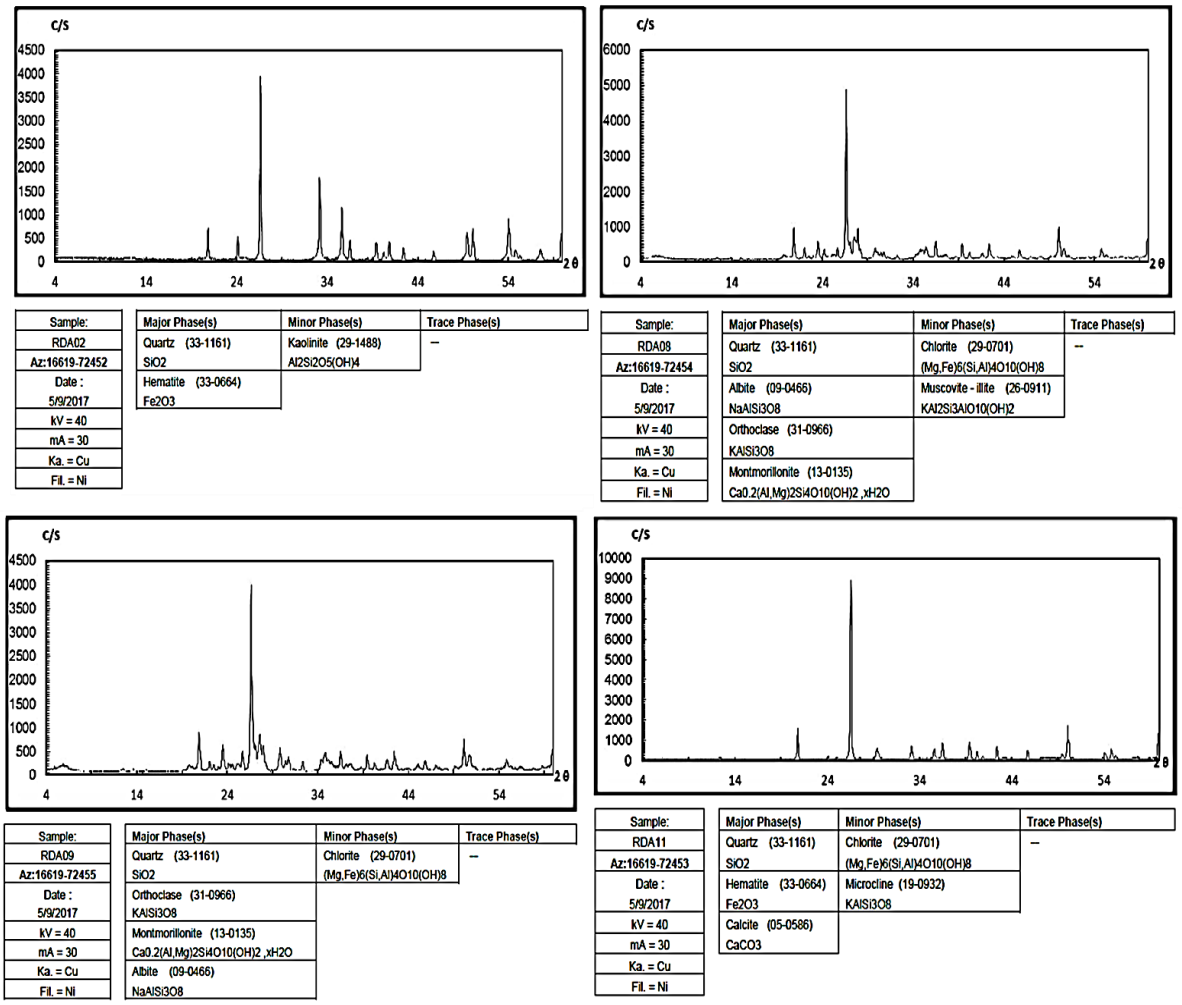

Fig 21. The results of XRD analysis of samples in the study area.

Actually, altered areas were enhanced in some parts of the west, south, and to a small extent in the northeast (Fig 9a, b). The result of band ratio (R=4/2 G=5/4 B=6/7) in OLI compared to ETM+ (R=3/1 G=5/7 B=4/3) due to masking out vegetation, was more widely used and interpreted in this area (Fig 9b). Altogether, the results of band ratio combinations in RGB for both Landsat-7 and 8 seem to be similar in their ability to target hydrothermal alteration mapping.

4.2. Result of Interpretation of ASTER

In this study, in order to identify the alteration zones, three methods (FCC, RBD and SAM) of ASTER processing were used and the results were presented in Figures 11 to 16. Based on false-color composite (FCC) method, 468 (RGB) was used in image processing ASTER. This FCC was indicated the minerals related to the propylitic alteration (epidote, chlorite) in green color which in the southeast was appeared. Also, the argillic alteration (clay minerals) in pink color was at the highest in the western, eastern, and central parts respectively (Fig 11). On the other hand, the relative absorption band depth (RBD) method was applied. The three RBD images were produced based on the absorption bands of each alteration spectra (Fig 13 to 15). Phyllic alteration enhances RBD6. This alteration is characterized by the main minerals of illite, muscovite (sericite) and quartz. Phyllic alteration in the center of the area was displayed the lowest value, but increases outside the study area in the east, west, and south of the region (Fig 13). RBD5 enhances argillic alteration. This alteration includes the main minerals of kaolinite, montmorillonite, and alunite. It was highlighted in the west, southwest, and north of the study area, as well as outside the study area in the northwest, north, and southeast (Fig 14). Finally, RBD8 characterizes propylitic alteration. Propylitic alteration consists of the main minerals of epidote, chlorite, and calcite. It was very weak within the study area except the west of the region. It was also appeared outside the study area in the western and southeastern parts (Fig 15). In spectral angle mapper (SAM) method, the spectrum of the spectrums related to the main minerals of the argillic and propylitic alteration outcrops in the region was used to prospecting similar spectral pixels. In this area, argillic alteration marked to a very small extent in the western

part of the study area, while outside the study area in the eastern, southern and northwestern parts was indicated a relative increase, respectively. Also, propylitic alteration increased in the northern, central and slightly southern parts, respectively, and was generally manifested by a decreasing trend from northwest to southeast (Fig 16).

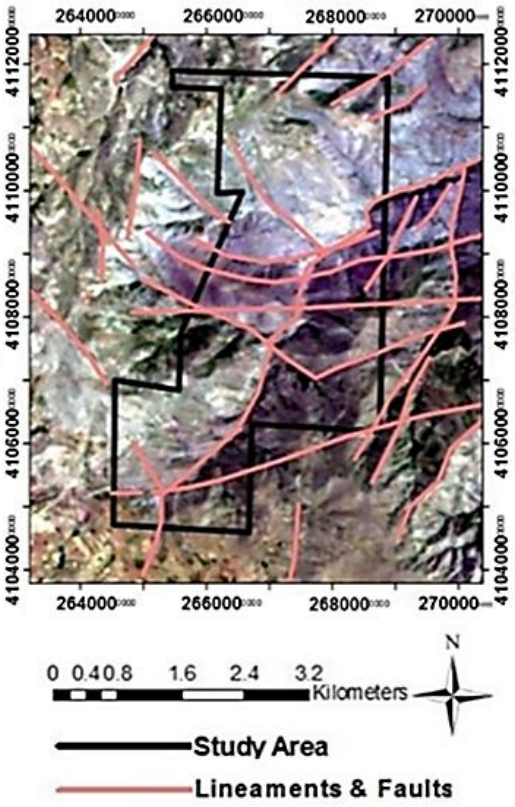

Fig 22. The lineaments map of Rashid-Abad mining area.

4.3. Result of Interpretation of Aeromagnetic

Total Magnetic Intensity (TMI) map was reduced to the dipole effect of the magnetic field and produced the reduction to the Pole (RTP) map. The RTP was removed the asymmetry at low latitudes magnetic anomalies and ensured that the anomalies were symmetrically centered over their causative sources (Fig 17a, b). Structural enhancement filters of aeromagnetic were applied to the RTP Map to place the edges and contacts of linear features. The edge detection techniques used in the study area consist of analytic signal (AS) and first vertical derivative (FVD) that have been extracted the lineaments (Fig 18a, b). Also, using these filters have been highlighted the anomaly bodies (Fig 18a, b).

4.4. Result of Field Observations

In order to compare the results of the satellite images processing and aeromagnetic data, the general condition of the area's structural and alterations were investigated using field observations and laboratory data. In the field investigations, the main fault which was called Rasht-Abad, was observed in the area (Fig 19a). Faults with NW- SE and NE-SW trends were also observed in the area (Fig 19b). In addition, due to the crushing of some stratigraphic units such as tuffs, high tectonic activity of the area were confirmed (Fig 19c).

The areas of iron- oxide, argillic, phyllic, propylitic, and silicic alterations were well observed on the surface. (Fig 23b-f). In order to investigate the alteration areas, some rock samples were selected and analyzed using two methods of microscopic (by thin sections) and X-ray diffraction (XRD). In the study of thin sections, most of the plagioclase coarse crystals, were became argillic and broken, then were composed in a fine-grained groundmass of plagioclases which had strongly mylonitized. They colored iron-hydroxides in the cross-section by dissolution as brownin in the path of mylonites. Also, due to the effect of tectonic tensions, the conditions for the alteration of coarse crystals were provided. However, argillic, phyllic (sericite), propylitic (chloritic), silicic and carbonate alterations were observed in thin sections (Fig 20a-c). X-ray diffraction analysis on the sample RDA02 was related to argillic alteration. RDA09 and RDA11 samples illustrated the propylitic alteration. Also, the RDA08 sample was related to phyllic (sericite) alteration. All the samples somehow indicated alterations in the study area. Figure 21 showed the results of X-ray diffraction analysis.

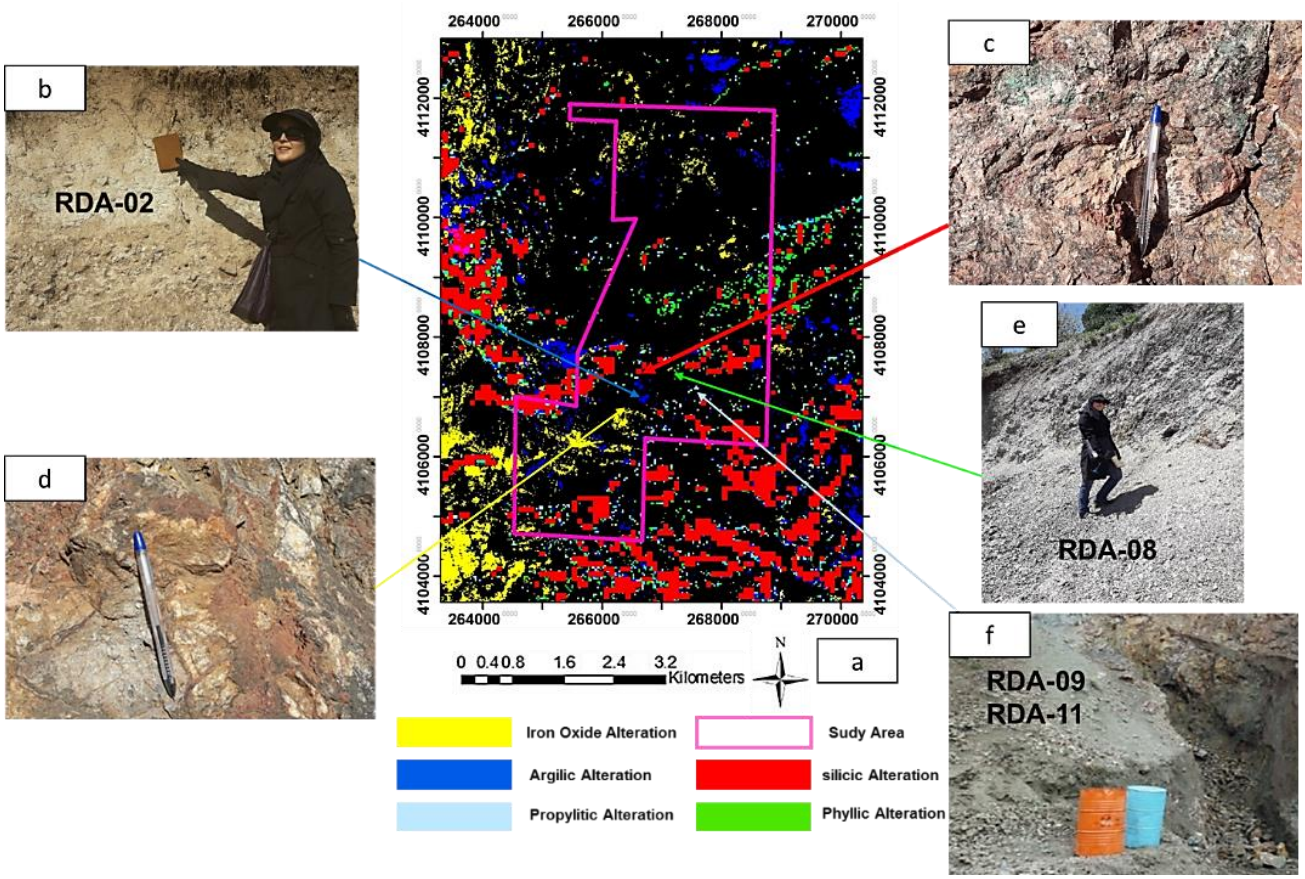

Fig 23. (a) The final map of alterations of Rashid-Abad mining area. (b) Argillic alteration in the field observations. (c) Silicic alteration in the field observations (main siliceous-brecciaed vein in the study area). (d) Iron Oxide alteration in the field observations. (e) Phyllic alteration in the field observations. (f) Propylitic alteration in the field observations.

4.5 Final Result of structural and alteration interpretation of the study area

Using a sun-angle filter on band 8 (panchromatic) of OLI for enhancement of sharp edges such as lineament and faults in the special direction was applied. The reason for selecting this band was the highest spatial resolution (15 meters) of this band comparing to other bands. For this purpose, in this study area, by applying the sun-angle filter in three radiation directions of N-S, SW, and SE, the lineaments with the E-W, NW-SE and NE-SW trends were enhanced, respectively. The most important lineament with the East-West trend was called Rasht-Abad fault (Fig 10a-c).

As mentioned earlier, one of the most important features of the analytic signal (AS) and first-Order vertical derivative (FVD) techniques is the identification of anomaly boundaries, magnetic lineaments, and hidden and obvious faults. In this study, magnetic lineaments were extracted using both filters of OLI and aeromagnetic data. Between two main anomalies (NW & W) in the study area, less magnetic field intensity was observed, which may be due to the existence of a major lineament with an E-W trend, which is most likely the same as the Rasht-Abad fault. In addition, there was another main lineament (NW-SE) in the northwest of the area with a high magnetic field, which was probably a passage for hydrothermal solutions to form minerals in the study area (Fig 17a, b).

Finally, using a sun-angle filter on band 8 (panchromatic) of OLI and also, AS and FVD filters on aeromagnetic data, lineaments and faults of the area were detected and investigated. The main fault Rasht-Abad (E-W) and the lineaments with the NW-SE and NE-SW trends were extracted using OLI, AS, and FVD filters, which were verified by the geology map and field investigations (Fig 19a, b). Eventually, using the combination of the extracted lineaments from the OLI image, AS and FVD aeromagnetic data, geological map and field observations, the final map of the lineaments and faults of the study area were prepared (Fig 22).

As previously stated, to study the alteration and target mineralization in the study area, different methods of images processing of Landsat 7, Landsat 8, and ASTER were used, and all the related alterations were extracted and investigated (Fig 6 to 16). Aeromagnetic data were also used to find anomaly bodies related to mineralization and alterations in the region and were extracted in the form of analytic signal (AS) and first-order vertical derivative (FVD) maps (Fig 17, 18). Generally, after using various methods of processing satellite images such

as BR, FCC, RBD, and SAM, and field and laboratory studies, which were already described in the relevant sections, the final map of alterations was prepared (Fig 23a). After preparing the final map of the alterations in the region, the alterations were compared to the magnetic anomalies extracted from the aeromagnetic map. Finally, iron oxide alterations in the region were related to low magnetic values. Argillic alterations were also correlated with moderate to increasing magnetic values. Also, argillic alterations, especially in the west of the study area were showed the highest positive correlation with magnetic values, where a major anomaly was located on a linear and narrow area with high magnetism (violet color), and with NW-SE trend. phyllic alterations in the east of the study area were corresponded to moderate magnetic values. Propylitic alterations did not show a significant relationship with magnetic values. Because they were associated with very low and moderate magnetic values in the AS and FVD maps, respectively. Silicic alterations also showed relatively high correlation with magnetic values in the region, because in the AS map only in the south and southeast were associated with very low magnetic values, and in the northwest of the region were revealed with moderate to increasing magnetic values. On the other hand, in the FVD map, they were associated with moderate to increasing magnetic values.

5. Conclusion

Integration of remote sensing and aeromagnetic data were applied to the investigation of structural features and alteration zones of the Rashid-Abad area. In regard to the structural features in the study area, using a sun-angle filter of OLI data and, AS and FVD filters of aeromagnetic data, have been detected two main lineaments in the area. The first main lineament is the same as the Rasht-Abad fault and the second major lineament is in the northwest of the region that is located in the study area with E-W and NW-SE trends, respectively. In fact, other lineaments with other trends in the area show that regional structures are controlled by both main structures of the region. Examination of the alterations responsible for mineralization using ETM +, OLI and especially ASTER satellite image processing methods and comparing them with the results of magnetic maps showed that the iron oxide alterations with negative magnetic anomalies, argillic and silicic alterations with moderate to increasing positive magnetic anomalies, phyllic alteration with moderate positive magnetic anomalies, and propylitic alteration does not also show a significant relationship with magnetic values. Therefore, in location of these magnetic anomalies, the extracted lineament and faults as controllers of the alteration zones are played an important role in mineralization in the study area. Finally, the activity of faults in periods of time has led to the mineralization phases and penetration of hydrothermal fluids. Eventually cross-linking between remote sensing and aeromagnetic data sets, and comparing the results with field observations and laboratory tests successfully localized mineralization within the study area.

References

Abedi M (2015): Reply to the comment by Ghobadipour B and Mojarradi B "Abedi M, Torabi SA, Norouzi GH, Hamzeh M, ELECTRE III: a knowledge-driven method for integration of geophysical data with geological and geochemical data in mineral prospectivity mapping, *Journal of Applied Geophysics* 117: 138-140.

Abedi M, Oskooi B (2015) A combined magnetometry and gravity study across Zagros orogeny in Iran, *Tectonophys* 664: 164-175.

Aghazadeh M, Castro A, Badrzadeh Z, Vogt K (2011) Post-collisional polycyclicplutonism from the Zagros hinterland. The Shaivar-Dagh plutonic complex Alborz belt. Iran, *Geological Magazine* 148: 980–1008.

Alavi M (1991) Sedimentary and structural characteristics of the Paleo-Tethys remnants in northeastern Iran, *Geological Society of America Bulletin* 103: 983-992.

Alimohammadi M, Alirezaei S, Kontak DJ (2015) Application of ASTER data for exploration of porphyry copper deposits: a case study of Daraloo–Sarmeshk area, southern part of the kerman copper belt, Iran, *Ore Geology Reviews* 70: 290–304.

Allen MB, Ghassemi, MR, Shahrabi, M, Qorashi, M (2003) Accommodation of late Cenozoic oblique shortening in the Alborz range, northern Iran, *Journal of Structural Geology* 25 (5): 659–672.

Amer, R, Kusky T, El Mezayen, A (2012) Remote sensing detection of gold-related alteration zones in Um Rus area, central eastern desert of Egypt, *Advances in Space Research* 49 (1): 121–134.

Arc GIS software, version 10.7.1© 2019 Esri, Creates 2D and 3D geographical analysis maps.

Arlegui LE, Soriano MA (1998) Characterizing lineaments from satellite images and field studies in the central Ebro basin (NE Spain), *International Journal of Remote Sensing* 19(16): 3169–3185.

Asiabanha A, Foden J (2012) Post-collisional transition from an extensional volcanosedimentary basin to a continental arc in the Alborz Ranges, *N-Iran*. Lithos 148: 98–111.

Azizi H, Jahangiri A (2008) Cretaceous subduction-related volcanism in the northern Sanandaj-Sirjan Zone, Iran, *Journal of Geodynamics* 45: 178-190.

Ballato P, Uba CE, Landgraf A, Strecker MR, Sudo M, Stockli DF, Friedrich A, Tabatabaei SH (2011) Arabia–Eurasia continental collision: insights from late Tertiary foreland-basin evolution in the Alborz Mountains, northern Iran, *Geological Society of America Bulletin* 123(1-2):106-131.

Baratian M, Arian MA, Yazdi A (2018) Petrology and petrogenesis of the SiahKuh intrusive Massive in the South of KhoshYeilagh, *Amazonia Investiga* 7 (17) : 616-629.

Brunet MF, Korotaev MV, Ershov AV, Nikishin AM (2003) The South Caspian Basin: a review of its evolution from subsidence modelling Sediment, *Sedimentary geology* 156: 119-148.

Carranza EJM, Sadeghi M (2010), Predictive mapping of prospectivity and quantitative estimation of undiscoveredVMS deposits in Skellefte district (Sweden), *Ore Geology Reviews* 38(3):219-241.

Crowley JK, Brickey DW, Rowan LC (1989) Airborne imaging spectrometer data of the Ruby Mountains, Montana: Mineral discrimination using relative absorption band-depth images, *Remote Sensing of Environment* 29(2): 121–134.

Dehnavi AG, Sarikhani R, Nagaraju D (2010) Image processing and analysis of mapping alteration zones in environmental research, East of Kurdistan, Iran, *World Applied Sciences Journal* 11(3): 278-283.

Doroozi R, Vaccaro C, Masoudi F, Petrini R (2016) Cretaceous alkaline volcanism in south Marzanabad, northern central Alborz, Iran: Geochemistry and petrogenesis, *Geoscience Frontiers* 7(6): 937-951.

Drury SA, Kelley SP, Berhe SM, Collier RE, Abraham M (1994) Structures related to Red Sea evolution in northern Eritrea, *Tectonics* 13(6):1371–1380.

El Khidir SO, Babikir IAA (2013) Digital image processing and geospatial analysis of Landsat 7 ETM+ for mineral exploration, Abidiya area, North Sudan, *International Journal of Geomatics and Geosciences* 3(3): 645–658.

El-Desoky HM, Soliman N, Heikal MA, Abdel-Rahman AM (2021), Mapping hydrothermal alteration zones using ASTER images in the Arabian–Nubian Shield: A case study of the northwestern Allaqi District, South Eastern Desert, Egypt, *Journal of Asian Earth Sciences* X, 5, 100060.

ENVI software, version 5.0© (2017) Provides image analysts with an image analysis platform.

ER Mapper software (ERDAS ER Mapper), version 2013© (2013) Providing advanced image processing and compression capabilities.

Evjen HM (1936) The place of the vertical gradient in gravitational interpretations, *Geophysics* 1(1): 127-136.

Fakhari S, Jafarirad A, Afzal P, Lotfi M (2019) Delineation of hydrothermal alteration zones for porphyry systems utilizing ASTER data in Jebal-Barez area, SE Iran. Iranian, *Journal of Earth Sciences* 11 (1): 80-92.

Faridi M, Anvari A (1996) Geological Map of Hashtjin Scale1:100,000: *Geological Survey of Iran*.

Frutuoso R, Lima A, Cláudia Teodoro A (2021) Application of remote sensing data in gold exploration: targeting hydrothermal alteration using Landsat 8 imagery in northern Portugal, *Arabian Journal of Geosciences* 14:459.

Geosoft Oasis Montaj software, version 7.2.1 (AS) © 2010, Open, share, and print Geosoft database files.

Gersman, R, Ben-Dor E, Beyth M, Avigad, D, Abraha M, Kibreab, A (2008) Mapping of hydrothermally altered rocks by the EO-1 hyperion sensor, northern danakil depression, Eritrea, *International Journal of Remote Sensing* 29 (13): 3911–3936.

Ghaeminejad H, Abedi M, Afzal P, Zaynali F, Yousefi M (2020) A fractal-based outranking approach for integrating geochemical, geological, and geophysical data, *Bollettino di Geofisica Teorica ed Applicata* 61(4): 555-588.

Githenya LK, Kariuki PC, Waswa AK (2019), Application of Remote Sensing in Mapping Hydrothermal Alteration Zones and Geological Structures as Areas of Economic Mineralization in Mwitika-Makongo Area, SE Kenya, *Journal of Environment and Earth Science* 9(11).

Han L, Liu Z, Ning Y, Zhao Z (2018) Extraction and analysis of geological lineaments combining a DEM and remote sensing images from the northern Baoji loess area, *Advances in Space Research* 62(9): 2480–2493.

Jayeoba A, Odumade D (2015) Geological and Structural Interpretation of Ado-Ekiti Southwest and its Adjoining Areas Using Aeromagnetic Data (Adapted from extended abstract prepared in conjunction with oral presentation given at Pacific Section *AAPG, SEG and SEPM Joint Technical Conference*, Oxnard, California.

Juteau T (2003) the ophiolites of Khoy (NW Iran): their significance in the Tethyan ophiolite belts of the Middle East, *Comptes rendus. Géoscience* 336 (2): 105–108.

Kalagari AA (1992) Principles of geophysical explorations, *saneibook* (Second edition) 485 p.

Kouhestani H, Azimzadeh AM, Mokhtari MAA, Ebrahimi M (2017) Mineralization and fluid evolution of epithermal base metal veins from the Aqkand deposit, NW Iran, *Neues Jahrbuch für Mineralogie-Abhandlungen* 194(2): 139–155.

Kruse F, Lefkoff A, Boardman J, Heidebrecht K, Shapiro A, Barloon P, Goetz A (1993) The spectral image processing system (SIPS) - interactive visualization and analysis of imaging spectrometer data, *Remote Sensing of Environment* 44:145-163.

Lawal AA, Abubakar AA, Victor AO (2021) Geophysical Investigation of a Fault Zone from Aeromagnetic Data over the Ageva Area of Okene Kogi State, Nigeria, *PHYSICSAccess* 1(1).

Li Q, Zhang B, Lu L, Lin Q (2014) Hydrothermal alteration mapping using ASTER data in Baogutu porphyry deposit, China, *35th International Symposium on Remote Sensing of Environment* (IOP) Conference Series: Earth and Environmental Science 17(1) 012174.

Li X (2008) Magnetic reduction-to-the-pole at low latitudes: Observations and considerations, *Journal of The Leading Edge* 27(8):990.

Manuel R, Brito MDG, Chichorro M, Rosa C (2017) Remote Sensing for Mineral Exploration in Central Portugal, *Minerals* 7(10):184.

Mars JC, Rowan LC (2006) Regional mapping of phyllic- and argillic-altered rocks in the zagros magmatic arc, Iran, using advanced Spaceborne thermal emission and

reflection radiometer (ASTER) data and logical operator algorithms, *Geosphere* 2 (3): 161–186.

Mars JC, Rowan LC (2010) Spectral assessment of new ASTER SWIR surface reflectance data products for spectroscopic mapping of rocks and minerals, *Remote Sensing of Environment* 114: 2011–2025.

Masoumi F, Ranjbar H (2011) Mapping of Hydrothermally Altered Areas Using ASTER and ETM+ Data in Northern Half of Baft Geological Map, *Journal of Geoscience* 20 (79):121-128.

Masoumi M, Honarmand M, Salimi A (2021) Integration of concentration-area fractal model and relative absorption band depth method for mapping hydrothermal alterations using ASTER data, *Remote Sensing Applications: Society and Environment*

Mehdikhani B, Imamalipour A (2021) ASTER-Based Remote Sensing Image Analysis for Prospection Criteria of Podiform Chromite at the Khoy Ophiolite (NW Iran), *minerals* 11(9): 960.

Mehrabi B, Ghasemi Siani M, Goldfarb R, Azizi H, Ganerod N, Marsh EE (2016) Mineral assemblages, fluid evolution, and genesis of polymetallic epithermal veins, Glojeh district, NW Iran, *Ore Geology Reviews* 78: 41–57.

Morelli M, Piana F (2006) Comparision between remote sensed lineaments and geological structures in intensively cultivated hills, Monferatto and Langhe domains, NW Italy, *International Journal of Remote Sensing* 27 (20): 4471-4493.

Nabavi MH (1976) Map of structural-sedimentary zones of Iran, *An introduction to the geology of Iran*, Geological Survey & Mineral Explorations of Iran (GSI).

Nabighian MN (1972) The analytic signal of two-dimensional magnetic bodies with polygonal cross section: its properties and use for automated anomaly interpretation, *International Journal of Geophysics* 37: 507-517.

Okoro EM, Onuoha KM, Okeugo CG, Dim CIP (2021) Structural interpretation of High-resolution aeromagnetic data over the Dahomey basin, Nigeria: implications for hydrocarbon prospectivity, *Journal of Petroleum Exploration and Production* 11: 1545–1558.

Pham LT, Oksum E, Le DV, Ferreira FJF, Le ST (2021) Edge detection of potential field sources using the softsign function, *Geocarto International* 36(1).

Rashmi S, Addamani S, Ravikiran A (2014) Spectral Angle Mapper Algorithm for Remote Sensing Image Classification, *JISET-International Journal of Innovative Science, Engineering & Technology 1:* 201-205.

Ritz JF, Nazari H, Ghassemi A, Salamati R, Shafei A, Solaymani S, Vernant P (2006) Active transtension inside central Alborz: A new insight into northern Iran–southern Caspian geodynamics, *Geology* 34 (6): 477–480.

Roest WR, Pilkington M (1993) Identifying remanent magnetization efects in magnetic data. *Geophysics* 58(5):653–659.

Rowan LC, Schmidt RG, Mars JC (2006) Distribution of hydrothermally altered rocks in the Reko Diq, Pakistan mineralized area based on spectral analysis of ASTER data. *Remote Sensing of Environment* 104: 74–87.

Sabins FF (1997) Remote Sensing, Principles and Interpretation, *3 ed, Freeman*, New York.

Sabins FF (1999) Remote sensing for mineral exploration, *Ore Geology Reviews* 14(3-4): 157-183.

Sadiya TB, Ibrahim O, Asma TF, Mamfe V, Nsofor CJ, Oyewmi AS, Ozigis MS (2014) Mineral detection and mapping using band ratioing and crosta technique in Bwari Area Council, Abuja Nigeria, *International Journal of Scientific and Engineering Research* 5(12): 1100-1108.

Salawu NB (2021) Aeromagnetic and digital elevation model constraints on the structural framework of southern margin of the Middle Niger Basin, Nigeria, *Scientific reports* 11(1): 1-12.

Salehi R, Saadi MN, Khalil A, Watanabe K (2015) Integrating remote sensing and magnetic data for structural geology investigation in pegmatite areas in eastern Afghanistan, *Journal of Applied Remote Sensing* 9(1): 096097.

Salem A (2005) Interpretation of magnetic data using analytic signal derivatives, *Geophys. Prospect* 53: 75-82.

Salem A, Ravat D, Mushayandebvu MF, Ushijima K (2004) Linearized least-squares method for interpretation of potential-field data from sources of simple geometry, *Geophysics* 69: 783-788.

Shi X, Al-Arifi N, Abdelkareem M, Abdalla F (2020) Application of remote sensing and GIS techniques for exploring potential areas of hydrothermal mineralization in the central eastern desert of Egypt, *Journal of Taibah University for Science* 14 (1): 1421–1432.

Solomon S, Ghebreab M (2006) Lineament characterization and their tectonic significance using Landsat TM data and field studies in the central highlands of Eritrea, *Journal of African Earth Sciences* 46(4): 371-378.

Srivastava S, Agarwal BNP (2010) Inversion of the amplitude of the two-dimensional analytic signal of magnetic anomaly by the particle swarm optimization technique, *Geophysical Journal International* 182(2): 652-662.

Stampfli GM (1996) The Intra-Alpine terrain: a Paleotethyan remnant in the alpine variscides *Eclogae Geologicae Helvetiae* 89: 13-42.

Teshnizi ES, Yazdi A, Golian M (2021) Remote Sensing Performance in Locating the Economic Veins of Robat Karim Manganese Mine, *Geotechnical Geology* 17 (2): 591-598.

Testa FJ, Villanueva C, Cooke DR, Zhang L (2018) Lithological and Hydrothermal Alteration Mapping of

Epithermal, Porphyry and Tourmaline Breccia Districts in the Argentine Andes Using ASTER Imagery, *Remote Sensing* 10(2): 203.

Thompson DT (1982) EULDPH: a new technique for making computer assisted depth estimates from magnetic data, *Geophysics* 47: 31–37.

Thurston JB, Smith RS (1997) Automatic conversion of magnetic data to depth, dip, and susceptibility contrast using the SPITM method, *Geophysics* 62: 807-813.

Yazdi A, Shahhosseini E, Moharami F (2022) Petrology and tectono-magmatic environment of the volcanic rocks of West Torud–Iran, *Iranian Journal of Earth Sciences* 14 (1): 40-57.

Yazdi Z, Rad AJ, Aghazadeh M, Afzal P (2018) Alteration mapping for porphyry copper exploration using ASTER and QuickBird multispectral images, Sonajeel Prospect, NW Iran, *Journal of the Indian Society of Remote Sensing* 46 (10): 1581-1593.

Zamyad M, Afzal P, Pourkermani M, Nouri R, Jafari MR (2019) Determination of Hydrothermal Alteration Zones Using Remote Sensing Methods in Tirka Area, Toroud, NE Iran, *Journal of the Indian Society of Remote Sensing* 47 (11): 1817-1830.